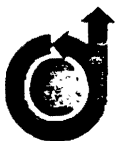# Nonequilibrium Effects in Oblique Shock-Wave Reflection

H. M. Glaz, P. Colella,
J. P. Collins, R. E. Ferguson

Nonequilibrium Effects in Oblique Shock-Wave Reflection

Harland M. Glaz*

University of Maryland, College Park, Maryland

Phillip Colella†

Lawrence Livermore National Laboratory, Livermore, California

and

James P. Collins‡ and Ralph E. Ferguson‡

U.S. Naval Surface Warfare Center, Silver Spring, Maryland

The Eulerian second-order Godunov scheme is extended to treat a mixture of nonequilibrium, chemically reacting gases and is implemented for high-temperature real air. Calculations of planar, oblique shock-wave reflections are presented and compared with experimental results and our previous gasdynamic simulations. In addition to being in better quantitative agreement with the experiments, the new results are found to reproduce many of the qualitative flowfield structures that are visible in the interferograms but that cannot be calculated from an equilibrium model.

Introduction

OBLIQUE shock-wave reflection is a benchmark problem, both for more complex physical and engineering problems and for validation of compressible flow computer codes.[1] This problem has proved amenable to accurate experimental measurement in shock tubes, and data are readily available in the literature. Also, the complex wave structure in the Mach stem region of these experiments closely resembles the flowfield phenomenology of typical applications. Finally, assuming inviscid gasdynamics, no length scale is present in the problem that has made it possible to propose analytical theories for important issues such as shock structure transition.[2]

The large shock-tube temperatures and pressures obtained for shock-wave Mach numbers (M_s) greater than about 5 necessitate low ambient density test gases (a few percent of atmospheric) for such experiments. Consequently, vibrational mode excitation can occur, and the associated relaxation length scale is comparable to hydrodynamic scales, e.g., the distance between the first and second triple point in a double Mach reflection or the triple-point height above the wedge surface. Additionally, if M_s is somewhat larger, the flowfield temperature is high enough (either behind the incident or reflected shock, or both) to introduce dissociation-recombination reactions in appropriate test gases; the postshock relaxation of the gas to its equilibrium value introduces other length scales, also comparable to hydrodynamic features.

High-resolution calculations of oblique shock-wave reflection flowfields using the Eulerian second-order Godunov scheme for gasdynamics have previously been reported.[1-6] These studies were inviscid and used (imperfect) equilibrium equations of state (EOS) to model high-temperature effects in the various gases. The agreement between experimental and computational results is excellent in these papers; however, real-gas Navier-Stokes calculations are required to reproduce

fully the flowfield phenomenology resulting from relaxation effects and the viscous boundary layer and to obtain better quantitative agreement.[1,2]

The purpose of this paper is to report an extension of our numerical approach to nonequilibrium, reactive gas mixtures applicable to multidimensional, high-temperature air flowfields. Our calculations are compared with experimental results obtained by I. I. Glass and his colleagues using the shock-tube facility at the University of Toronto Institute for Aerospace Studies (UTIAS).[2] For the cases studied here, the test gas is air, and the shocks are sufficiently strong to induce significant vibrational nonequilibrium in critical regions of the flowfield; we are also able to validate substantial chemistry effects in some of the cases.

The high-temperature air model used here is expected to be valid only to temperatures up to 8000-9000 K because we include only vibrational excitation and a dissociation-recombination reaction mechanism. The algorithm could be extended, however, to include additional physical effects such as ionization. In particular, we expect that the mathematical structure supports the physics needed for application in re-entry aerodynamics.

Oblique Shock-Wave Reflection

The configuration for oblique shock-wave reflection is illustrated in Figs. 1 and 2. In Fig. 1, a planar shock wave of shock-wave Mach number M_s approaches, through quiescent gas, the wedge corner that is set at an angle θ_w with respect to the incoming flow. For inviscid equilibrium flow, there is no length scale in the problem, which implies that the solution depends only on x/t and y/t (where the wedge corner is taken as the origin of coordinates), and the resulting flowfields are called pseudosteady or self-similar. The possible solutions[2] are illustrated in Fig. 2; they are functions of M_s, θ_w, the EOS of the gas, and, for a nonpolytropic EOS, the preshock state of the gas.[1,2]

The data obtained from the UTIAS facility are in the form of infinite fringe interferograms of the flowfield, obtained with a 23-cm-diam field-of-view Mach-Zender interferometer.[7] The density jump $\Delta\rho$ between fringes in the interferogram is a constant, allowing for easy data reduction. However, the shock jump conditions must be evaluated to obtain states (1), (2), (3) at the triple point since the fringes inside the shock waves cannot be resolved. For a frozen or equilibrium jump, this

problem is straightforward, given an accurate measurement of the triple-point angle χ.[2,7,9]

Relaxation processes introduce two characteristic signatures into the the interferograms. First, the relaxation zone behind the incident shock is readily apparent. Second, the fringes behind the reflected shock are nearly tangentially incident at the shock. Of course, the physical mechanisms responsible for the relaxation effects cannot be discerned from the interferograms alone, and additional analysis or computation is required. With relaxation processes present, length scales are introduced, and the solution is no longer self-similar. Among other effects, it becomes possible for the triple-point angle χ to be time-dependent. Also, it is possible that the shock layers in the problem are only partially frozen at scales resolvable in the interferograms. As a consequence, the triple-point analysis using either frozen or equilibrium jump conditions may introduce errors into the data reduction.

If ℓ represents a relaxation length scale and L (see Fig. 2) a hydrodynamic scale, $\ell \gg L$, $\ell \sim L$, and $\ell \ll L$ represent frozen, nonequilibrium, and equilibrium flow, respectively. A time-dependent experiment or calculation runs through each of the three regimes in succession as $t \to \infty$. It has been shown convincingly that significant flowfield features (e.g., χ) differ substantially in the two asymptotic regimes that can be studied by gasdynamic computations.[1,3,4] The problems studied here are all in the nonequilibrium regime.

Equations of Motion

High-temperature air is modeled as a nonequilibrium, reacting mixture of gases. For the conditions (i.e., temperature range) treated in this paper, and ignoring ionization reactions, the governing equations in conservation form are:[10]

$$\rho_t^\alpha + \nabla \cdot (\rho^\alpha \mathbf{u}) = \dot{w}^\alpha, \qquad \alpha = 1,...,N \tag{1}$$

$$(\rho \mathbf{u})_t + \nabla \cdot (\rho \mathbf{u} \cdot \mathbf{u} + p) = 0 \tag{2}$$

$$(\rho E)_t + \nabla(\rho \mathbf{u} E + \mathbf{u}p) = -\Sigma_\alpha \dot{w}^\alpha (\Delta h_f^0)^\alpha \tag{3}$$

$$(\rho^\alpha q^\alpha)_t + \nabla \cdot (\rho^\alpha q^\alpha \mathbf{u}) = \rho^\alpha \dot{q}^\alpha, \qquad \alpha = 1,...,N \tag{4}$$

where ρ^α = density of species α, $\rho \equiv$ mixture density $= \Sigma_\alpha \rho^\alpha$, $\mathbf{u}$ = velocity, p = pressure, E = total energy per unit mass, q^α = vibrational energy per unit mass of species α, (Δh_f^0) = specific heat of formation at 0 K of species α, and N = total number of species present. The source terms $\dot{w}^\alpha$ and $\dot{q}^\alpha$ represent the production of species α through chemical reaction and the relaxation of vibrational energy of species α to its equilibrium value, respectively.

The pressure is given by the equation of state

$$p = \rho \bar{R} T \tag{5}$$

where T = temperature, $\bar{R} = R/M$, R = universal gas constant, $M = (\Sigma_\alpha c^\alpha/M^\alpha)^{-1}$, M^α = molecular weight of species α, and $c^\alpha \equiv$ mass fraction of species $\alpha = \rho^\alpha/\rho$. The total specific energy is
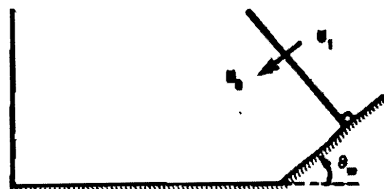
$$E = e + \frac{1}{2}\mathbf{u}^2 \tag{6}$$

where e = specific internal energy of the mixture, i.e., $e = \Sigma_\alpha c^\alpha e^\alpha$, with e^α = specific internal energy of species α,

$$e^\alpha = (\gamma^\alpha - 1)^{-1} R^\alpha T + q^\alpha \tag{7}$$

Here, $R^\alpha = R/M^\alpha$ and γ^α = polytropic index for species α(= 7/5 for diatomic species and 5/3 for monatomic species). The first term on the right-hand side of Eq. (7) represents the contribution of translational and rotational modes (which are assumed to be in equilibrium) to the internal energy. It follows from Eq. (7) that

$$T = \left(e - \sum_\alpha c^\alpha q^\alpha\right) \Big/ \sum_\alpha \frac{c^\alpha R^\alpha}{\gamma^\alpha - 1} \tag{8}$$

Substituting Eq. (8) into Eq. (5), one readily sees that the pressure is a function of the conserved quantities.

Conservation of mass implies that

$$\rho_t + \nabla \cdot (\rho \mathbf{u}) = 0 \tag{9}$$

i.e., $\Sigma_\alpha \dot{w}^\alpha = 0$. Equations (1) and (4) can be recast for smooth flow into the characteristic forms

$$c_t^\alpha + \mathbf{u} \cdot \nabla c^\alpha = \rho^{-1} \dot{w}^\alpha, \qquad \alpha = 1,...,N \tag{10}$$

$$(c^\alpha q^\alpha)_t + \mathbf{u} \cdot \nabla(c^\alpha q^\alpha) = c^\alpha \dot{q}^\alpha, \qquad \alpha = 1,...,N \tag{11}$$

Note that $\Sigma_\alpha c^\alpha = 1$ and that only N of the $N + 1$ equations (9) and (10) are independent.
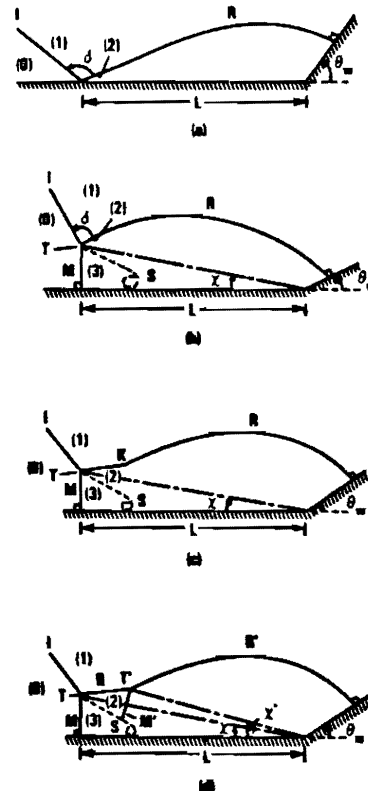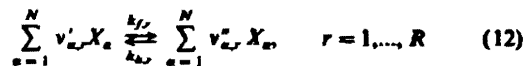
Fig. 2 Schematic diagrams of oblique shock-wave reflection types: a) regular reflection (RR); b) single Mach reflection (SMR); c) complex Mach reflection (CMR); d) double Mach reflection (DMR). States (0), (1), (2), and (3) satisfy the reflection or triple-point jump conditions. Other standard terminology used in the text is χ = triple-point angle, T = triple point, R = reflected shock, I = incident shock, M = Mach stem, T' = second triple point, χ' = second triple-point angle, M' = second Mach stem, and K = kink.

Fig. 1 Schematic diagram for flowfield initialization.

For high-temperature air without ionization, it is a reasonable approximation[11] to take $N = 5$ corresponding to the species O_2, N_2, NO, O, and N. Following Ref. 11, we assume that the reaction mechanism consists of R elementary reactions of the form

$$\sum_{\alpha=1}^{N} v'_{\alpha,r} X_\alpha \underset{k_{b,r}}{\overset{k_{f,r}}{\rightleftharpoons}} \sum_{\alpha=1}^{N} v''_{\alpha,r} X_\alpha, \quad r = 1,\dots, R \quad (12)$$

where X_α = molar concentration of species α, $v'_{\alpha,r}$ and $v''_{\alpha,r}$ are the stoichiometric coefficients for species α in reaction r, and $k_{f,r}$ and $k_{b,r}$, which are experimentally determined explicit functions of T, are the forward and backward reaction rates, respectively. The production terms are[11]

$$\dot{w}^\alpha = M^\alpha \dot{X}_\alpha, \quad \alpha = 1,\dots, N \quad (13)$$

where

$$\dot{X}_\alpha = \sum_{r=1}^{R} (v''_{\alpha,r} - v'_{\alpha,r})$$

$$\cdot \left\{ k_{f,r}(T) \prod_{s=1}^{N} X_s^{v'_{s,r}} - k_{b,r}(T) \prod_{s=1}^{N} X_s^{v''_{s,r}} \right\} \quad (14)$$

For the calculations presented in this paper, the reaction mechanism and the functional form of $k_{f,r}$, $k_{b,r}$, follow the data given by Park.[12,13]

Finally, relaxation of vibrational energy is modeled by

$$\dot{q}^\alpha = \frac{q^{*,\alpha}(T) - q^\alpha}{\tau^\alpha(p,T)}, \quad \alpha = O_2, N_2, NO \quad (15)$$

where $q^{*,\alpha}(T)$ = equilibrium vibrational energy per unit mass of species α at temperature T and τ^α = relaxation time. The monatomic species O, N do not possess vibrational modes, so $q^\alpha \equiv 0$ for $\alpha = $ O, N. These terms are given explicitly by[11]

$$q^{*,\alpha}(T) = \frac{R^\alpha \theta_0^\alpha}{\exp(\theta_0^\alpha/T) - 1}, \quad \alpha = O_2, N_2, NO \quad (16)$$

where θ_0^α = vibrational temperature for species α, and

$$\tau^\alpha(p,T) = \frac{B^\alpha \exp[(k^\alpha/T)^{\frac{1}{3}}]}{p} \quad (17)$$

The equation for τ^α is an approximate form of the Landau-Teller equation valid in the temperature range considered here.[11] The constants B^α, k^α must be experimentally determined; we are using the data from Ref. 11 with the additional approximation that the heat bath molecule for species α is taken to be species α (in general, the constants depend on the collision partner).

Numerical Method

An operator splitting approach has been implemented in which the gasdynamics with frozen chemistry is solved for Δt, alternately with the chemistry advanced Δt at constant volume and ignoring spatial gradients. The time step Δt is chosen to satisfy the CFL condition for the gasdynamic scheme alone. For general reactive flow problems, such a method potentially introduces large errors due to the ignored hydrodynamic-chemistry interactions over a time step, unless the spatial mesh in reaction regions is small enough to bring the two time scales into balance. Our working hypothesis for the present work is that, because both the vibrational relaxation and dissociation-recombination processes tend to equilibrium without large oscillations, the method will be accurate on length scales greater than a few mesh points, even on relatively coarse meshes.

The hydrodynamic step is solved with a version of the Eulerian second-order Godunov scheme.[4] This scheme is directionally split, so that we discuss the method for solving one-dimensional gasdynamics in Cartesian coordinates. A brief summary of the method is as follows: 1) characteristic variables are selected and high-order, monotonized slopes are constructed for them in each computational zone; 2) left and right states at each zone interface are constructed by applying characteristic projection operators to the profiles constructed in the first step; 3) the zone interface Riemann problems are solved; and 4) interface fluxes are evaluated and a conservative differencing step performed. The modifications necessary to generalize the single-phase method to a gas mixture satisfying Eqs. (1–8) are straightforward, as indicated in the following (the ensuing discussion assumes familiarity with Ref. 4).

There are several natural choices for characteristic variables, e.g., $v' = (\rho^1,\dots,\rho^N,u,p,q^1,\dots,q^N)^T$, $v'' = (\tau,\rho^1,\dots,\rho^{N-1}, u,p,q^1,\dots,q^N)^T$, $\tau = \rho^{-1}$, etc. For the present study, we have chosen

$$v = (\tau, c^1,\dots, c^N, u, p, q^1,\dots, q^N)^T \quad (18)$$

subject to the constraint $\sum_\alpha c^\alpha = 1$ everywhere; the constraint allows us both to retain τ and not to single out any of the c^α in the characteristic transport step. For this choice, the characteristic equations for the variables $c^\alpha, q^\alpha, \alpha = 1,\dots, N$ [see Eqs. (10) and (11)] decouple from the rest of the system. Consequently, computation of the characteristic projection operators is almost exactly as described in Ref. 4, and these operators have the same properties. The mixture Riemann problem has essentially the same solution as that for single-fluid gasdynamics. This is so because the quantities c^α, q^α are advected along streamlines and do not jump across the nonlinear waves (shock waves and rarefaction waves) in the Riemann problem solution. Thus, only τ, u, and p vary across the left and right waves, and the Rankine-Hugoniot conditions are as in the single-fluid case. If γ is defined via $p = (\gamma - 1)\rho(e - \sum_\alpha q^\alpha)$, it is easy to check that γ also does not jump across nonlinear waves. Also, $\Gamma = \gamma$, where the "sound speed gamma" is defined by $c^2 = \Gamma p \tau c$ = (frozen) sound speed. Of course, the value of γ is different in the left and right states defining the Riemann problem. The end result is that the nonlinear secant iteration and the sampling procedure to obtain interface values is identical to that described in Ref. 4, save for the additional bookkeeping required to keep track of all of the components of v.

The set of equations solved in the chemistry step of the operator splitting algorithm is

$$\frac{dc^\alpha}{dt} = \rho^{-1} M^\alpha \dot{X}_\alpha, \quad \alpha = 1,\dots, N \quad (19)$$

$$\frac{d(c^\alpha q^\alpha)}{dt} = c^\alpha \frac{q^{*,\alpha}(T) - q^\alpha}{\tau^\alpha(p,T)}, \quad \alpha = N_2, O_2, NO \quad (20)$$

Table 1 Quantitative comparisons of overall flowfield structure

Case		χ	χ'	δ
I	Exp.	11.5		32.0
	Hansen	12.0		29.5
	VR	12.4		31.5
	CR + VR	11.6		31.0
II	Exp.	7.5	7.8	23.0
	Hansen	9.6	9.0	33.5
	VR	10.0	10.2	31.5
	CR + VR	8.2	8.5	24.0
III	Exp.	10.0	11.2	21–23
	Hansen	12.2	12.5	27.0
	VR	12.4	13.2	28.5
	CR + VR	10.4	11.4	23.6

EQUILIBRIUM EOS (HANSEN)

NONEQUILIBRIUM WITHOUT REACTION
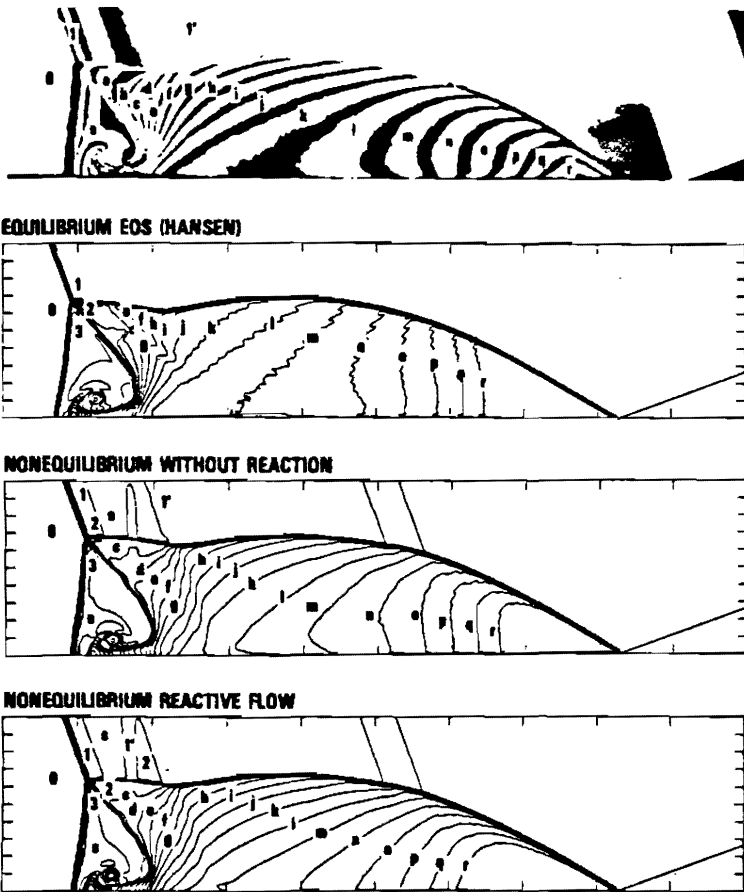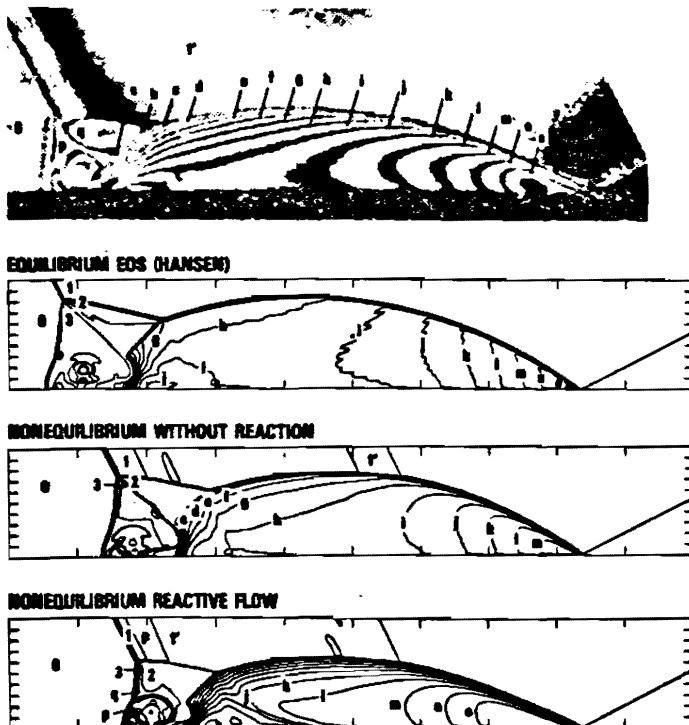

NONEQUILIBRIUM REACTIVE FLOW

Fig. 3 $M_\infty = 7.19$, $\theta_w = 20$ deg. The interferogram from the experiment is shown on top, followed by density (ρ/ρ_0) contour plots for the three calculations. The top two figures are reproduced from Ref. 3, p. 196. The values of ρ/ρ_0 are:

0	1.00	3	5.59	d	7.94	h	9.24	l	10.53	p	11.82
1	5.47	a	6.97	e	8.27	i	9.56	m	10.85	q	12.15
1'	6.13	b	7.30	f	8.59	j	9.88	n	11.18	r	12.47
2	6.65	c	7.62	g	8.91	k	10.21	o	11.50	s	5.91

EQUILIBRIUM EOS (HANSEN)

NONEQUILIBRIUM WITHOUT REACTION
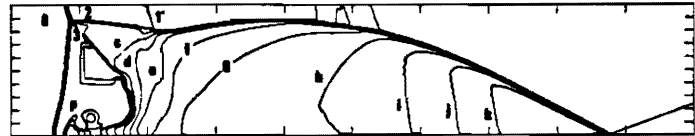

NONEQUILIBRIUM REACTIVE FLOW

Fig. 4 $M_\infty = 8.70$, $\theta_w = 27$ deg. The interferogram from the experiment is shown on top, followed by density (ρ/ρ_0) contour plots for the three calculations. The two top figures are reproduced from Ref. 3, p. 190. The values of ρ/ρ_0 are:

0	1.00	3	5.74	d	11.42	h	13.95	l	16.47	o	18.36
1	5.63	a	9.53	e	12.05	i	14.58	m	17.10	p	6.37
1'	6.89	b	10.16	f	12.68	j	15.21	n	17.73	q	8.07
2	7.44	c	10.79	g	13.32	k	15.84				

EQUILIBRIUM EOS (HANSEN)

NONEQUILIBRIUM WITHOUT REACTION

NONEQUILIBRIUM REACTIVE FLOW

Fig. 5 $M_s = 8.86$, $\theta_w = 20$ deg. The interferogram from the experiment is shown on top, followed by density (ρ/ρ_0) contour plots for the three calculations. The two top figures are reproduced from Ref. 3, p. 203. The values of ρ/ρ are:

0	1.00	3	5.72	d	9.43	g	11.37	j	13.31	m	15.25
1	5.64	a	7.50	e	10.08	h	12.02	k	13.95	n	15.89
1'	6.93	b	8.14	f	10.73	i	12.66	l	14.60	p	6.85
2	6.85	c	8.79								
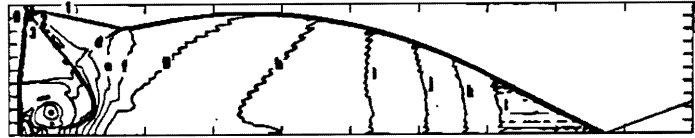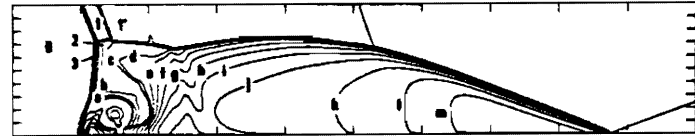
$$\frac{de}{dt} = \rho^{-1} \sum_\alpha \{M^\alpha (\Delta h_j^0)^\alpha\} \dot{X}_\alpha \qquad (21)$$

This is a system of $N + 4$ coupled, nonlinear, ordinary differential equations; note that T, p are explicit functions of c^α, $c^\alpha q^\alpha$, $\alpha = 1,..., N$, and e according to the relations (5) and (8). They are in a form suitable for solution by standard numerical methods. In our calculations, we have used standard explicit solvers, such as second- and fourth-order Runge-Kutta methods or Euler's method. The chemistry time step was taken small enough to insure accuracy. In future work, we intend to explore implicit methods, stiff solvers, and various approximation schemes that take advantage of the probability that, for much numerical work, accuracy at levels higher than the hydrodynamic scheme may not be useful.

Initial and Boundary Conditions

A square mesh aligned with the wedge surface (Fig. 1) is used. The ambient state U_0 is taken to consist of 79% N_2 and 21% O_2 at density ρ_0 and pressure p_0, corresponding to the experimental data[3] for each calculation. The postshock state U_1 is obtained by solving the Rankine-Hugoniot conditions with an additional equation enforcing vibrational equilibrium. The jump is then conservatively interpolated onto the mesh, and the calculation runs to completion without further intervention.

The structure of the one-dimensional incident shock is an important issue in our analysis of the results. The reactive flow calculations exhibit an "overshoot" behind the shock prior to downstream relaxation to equilibrium (and this has been verified by long-time calculations on a one-dimensional mesh); this phenomenon may well be physical. Nevertheless, a small-amplitude disturbance is introduced into the flow behind the reflected shock at the second triple point by the overshoot. The calculated incident shock is partially reactive on scales of the order of a few mesh points, whereas the data reduction for the

experiment assumes a frozen jump; on the fine meshes used here, the error introduced by this difference is small and would be made smaller by refining the mesh still further. Both of these issues can be resolved by using another version of the Godunov scheme in which the incident shock is treated as a tracked front;[14] this will be the subject of further work, along with computing the exact steady shock structure (for both frozen and partial reaction jumps) by quadrature.

The only nontrivial boundary condition is at the top. We have implemented a Dirichlet condition in which a discontinuous jump is imposed at the (known) intersection of the incident shock with the top boundary. The postshock state is chosen to be the currently available value from the downstream edge of the state (1) region (the reaction process continues here throughout the calculation). The boundary has been taken far enough away from the reflected shock so that the error introduced by this procedure is negligible. Nevertheless, for reasons of efficiency, we expect to implement a true Dirichlet condition (see, e.g., the treatment in Ref. 15) in future work.

For the meshes used in obtaining the results, the length L (see Fig. 2) corresponds to 350-400 zones, and the vertical distance between the wedge surface and the top of the reflected shock contains between 60 and 100 zones. This is comparable, but somewhat coarser, than the meshes used in Ref. 3. The mesh interval $\Delta x = \Delta y$ is chosen so that at the end of the calculation, L corresponds closely to the experiment.

Results

Results have been obtained for three cases: (I) $M_s = 7.19$, $\theta_w = 20$ deg; (II) $M_s = 8.70$, $\theta_w = 27$ deg; and (III) $M_s = 8.86$, $\theta_w = 20$ deg. Two calculations have been performed for each of the cases: a vibrationally relaxing, nonreactive calculation (VR) and a vibrationally relaxing, reactive calculation (CR + VR). A direct comparison of the flowfield density contour levels of these computations with experimental data and previously reported calculations[3] with an equilibrium EOS is
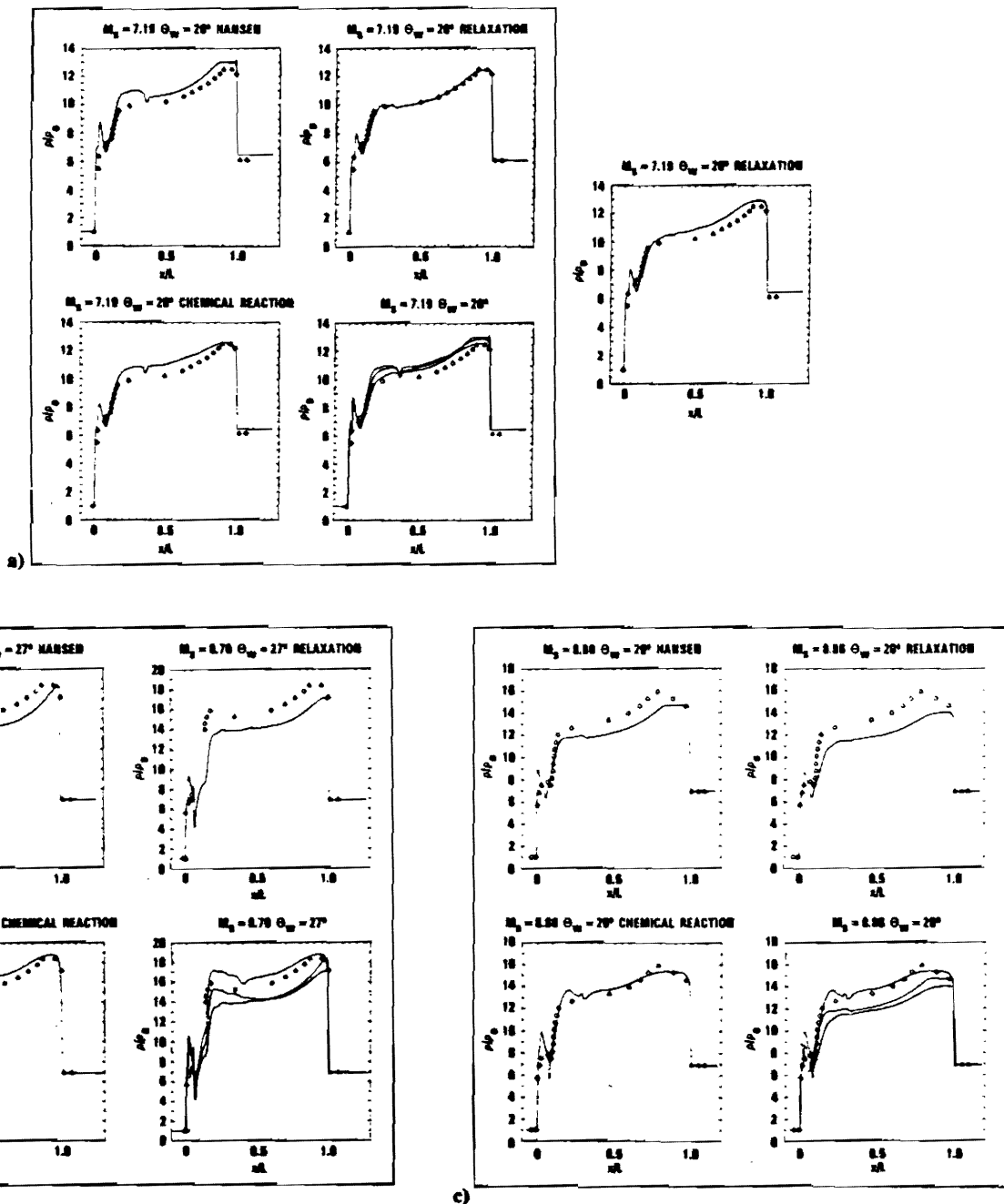
Fig. 6   Plots of density vs distance along the wedge surfaces for the three cases. See Figs. 1 and 2 for definitions of ρ_0, L. The extra plot for case I corresponds to the calculation with a forced match in state 1'. Diamonds represent experimental data.

made in Figs. 3–5 for the three cases. The EOS used in the gasdynamic calculation is a modified[7] version of the Hansen EOS.[16] The overall structure of the configurations may be discerned by comparing the triple-point angles, χ, χ', and δ = corner attachment angle (in degrees; all measurements are by hand) in Table 1. It is quite clear that the comparison improves substantially as one moves down the page in these figures; the degree of tangential incidence of the contours at the reflected shock improves and matches the interferogram in the reactive case, and Table 1 shows that wave structure fidelity requires reactive flow calculations (since the Hansen EOS includes reaction effects, it can actually be better than the relaxing, nonreactive model). For cases II and (especially) III, a wave is introduced into the disturbed flow at T' that is not present in the experiment; this small amplitude disturbance is

caused either by an overshoot behind the incident shock wave or the error in our top boundary condition procedure. Quantitatively, the contours are off by about two levels. It is possible that this can be fully explained by the assumption of a frozen triple point in the data reduction for the interferogram. None of the new calculations match this condition on scales comparable with the mesh. Whether a substantial mesh refinement (or a tracked incident shock) is required for convergence or whether the experimental incident shock should be taken as partially relaxed/reactive is not clear.

Wall density plots for the calculations are presented in Fig. 6. The "wall heating" numerical layer, already present for gasdynamic results,[1,3] is intensified here (this is easily seen in the contour plots, as well), and we have sometimes used the results from the second row of zones above the wedge surface.

For case I, it may be noted that there is a mismatch between the data points in state 1' and the value computed for this state in the calculations. An additional computation was made in which agreement for this value was forced, and these results are presented as well. In light of these factors, the agreement is good overall, and some of the remaining discrepancies can be analyzed in terms of boundary-layer effects in the experiments.[1,3]

Details of the Mach stem region are illustrated in Fig. 7. These plots illustrate the rich structure of the mixing processes induced by the wall jet-vortex rollup interaction[1] in this part of the flowfield.

A striking feature of the new computations is the excellent qualitative agreement in the Mach stem region. For example, in Fig. 5, contours c (respectively, a and b) in the reactive flow plot may be compared with the structures near contour a (respectively, p) in the interferogram. It may, therefore, be concluded that these features are indeed nonequilibrium effects. In summary, the new scheme presented here has been shown to be capable of reproducing all of the major dynamic features of planar oblique shock-wave reflection and has demonstrated that accurate modeling of the time-dependent relaxation and reaction processes are necessary for their determination. A complete simulation capability still requires implementation of a Navier-Stokes capability in the boundary layer in order to eliminate the wall heating effect and to improve further the modeling of the vortex rollup.
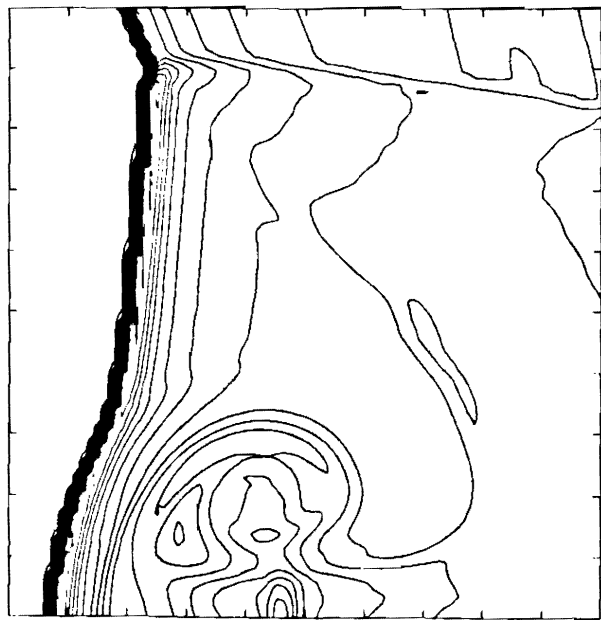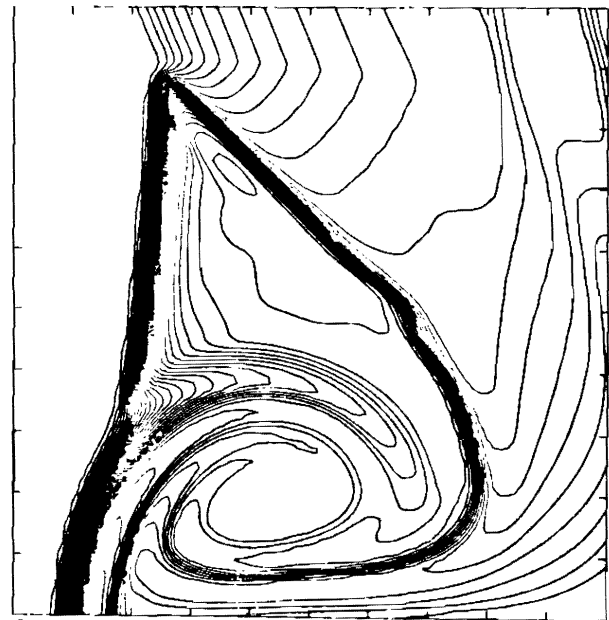
MASS FRACTION OF 0

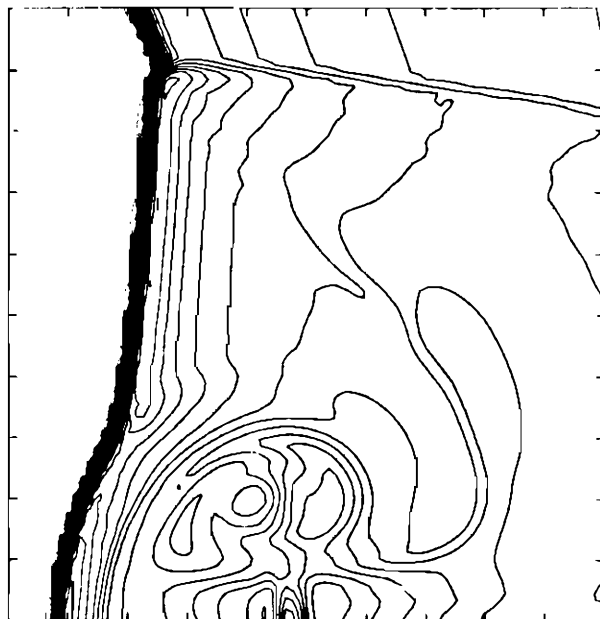**MASS FRACTION OF N$_2$**

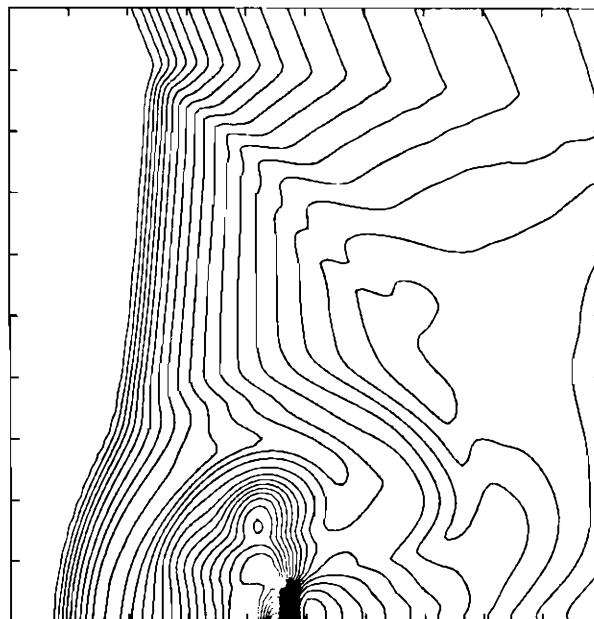**TEMPERATURE**

MASS FRACTION OF O$_2$

Fig. 7 Blowup plots of the Mach stem region for case III. These plots all use 30 equally spaced contours.

VIBRATIONAL ENERGY FOR O$_2$ **VIBRATIONAL ENERGY FOR N$_2$**

e)   f)

Fig. 7   Continued; blowup plots of the Mach stem region for case III.

Acknowledgments

References

[1]Glaz, H. M., Colella, P., Glass, I. I., and Deschambault, R. L., "A Numerical Study of Oblique Shock-Wave Reflections with Experimental Comparisons," *Proceedings of the Royal Society of London, Series A*, Vol. 398, March 1985, pp. 117–140.

[2]Glass, I. I., "Some Aspects of Shock-Wave Research" (Dryden Lecture), *AIAA Journal*, Vol. 25, Feb. 1987, pp. 214–229.

[3]Glaz, H. M., Colella, P., Glass, I. I.. and Deschambault, R. L., "A Detailed Numerical, Graphical and Experimental Study of Oblique Shock Wave Reflections," Lawrence Berkeley Laboratory, Berkeley, CA, LBL-20033, April 1985.

[4]Colella, P. and Glaz, H. M., "Efficient Solution Algorithms for the Riemann Problem for Real Gases," *Journal of Computational Physics*, Vol. 59, June 1985, pp. 264–289.

[5]Colella, P. and Glaz, H. M., "Numerical Computation of Complex Shock Reflections in Gases," *Proceedings of the Ninth International Conference on Numerical Methods in Fluid Dynamics*, edited by Soubaramayer and J. P. Boujot, *Lecuture Notes in Physics*, Vol. 218, Springer-Verlag, New York, 1985.

[6]Glaz, H. M., Glass, I. I., Hu, T. C. J., and Walter, P., "Oblique Shock Wave Reflections in SF$_6$: A Comparison of Calculation and Experiment," *Progress in Astronautics and Aeronautics: Dynamics of Explosions*, Vol. 106, edited by J. R. Bowen, J.-C. Leyer, and R. I. Soloukhin, AIAA, New York, 1986, pp. 359–387.

[7]Deschambault, R. L., "Nonstationary Oblique Shock Wave Reflections in Air," Institute for Aerospace Studies, Univ. of Toronto, Toronto, Canada, Rept. 270, 1984.

[8]Deschambault, R. L. and Glass, I. I., "An Update on Nonstationary Oblique Shock Wave Reflections: Actual Isopycnics and Numerical Experiments," *Journal of Fluid Mechanics*, Vol. 131, June 1983, pp. 27–57.

[9]Ben-Dor, G. and Glass, I. I., "Domains and Boundaries of Non-Stationary Oblique Shock Wave Reflections. 1. Diatomic Gas," *Journal of Fluid Mechanics*, Vol. 92, Pt. 3, 1979, pp. 459–496; also, "Domains and Boundaries of Non-Stationary Oblique Shock Wave Reflections. 2. Monatomic Gas," *Journal of Fluid Mechanics*, Vol. 96, Pt. 4, 1980, pp. 735–756.

[10]Anderson, J., *Modern Compressible Flow with Historical Perspective*, McGraw-Hill, New York, 1982.

[11]Vincenti, W. G. and Kruger, C. H., *Introduction to Physical Gas Dynamics*, R. E. Krieger Publishing, Huntington, NY, 1975.

[12]Park, C., "Problems of Rate Chemistry in the Flight Regimes of Aeroassisted Orbital Transfer Vehicles, *Progress in Astronautics and Aeronautics: Thermal Design of Aeroassisted Orbital Transfer Vehicles*, Vol. 106, edited by H. F. Nelson, AIAA, New York, 1985, pp. 511–537.

[13]Park, C., "On Convergence of Computational Chemically Reacting Flow," AIAA Paper 85-0247, 1985.

[14]Chern, I.-L. and Colella, P., "A Conservative Front Tracking Method for Hyperbolic Conservation Laws," Lawrence Livermore National Laboratory, Livermore, CA, UCRL-97200, July 1987.

[15]Colella, P., Ferguson, R. E., Glaz, H. M., and Kuhl, A. L., "Mach Reflection from HE-Driven Blastwave," *Progress in Astronautics and Aeronautics: Dynamics of Explosions*, Vol. 106, edited by J. R. Bowen, J.-C. Leyer, and R. I. Soloukhin, AIAA, New York, 1986, pp. 388–421.

[16]Hansen, C. F., "Approximations for the Thermodynamic and Transport Properties of High-Temperature Air," NASA TR R-50, 1959.